ACS NANO
Cite This: ACS Nano 2018, 12, 11561−11571
www.acsnano.org

ARTICLE

Triboelectric Self-Powered Wearable Flexible Patch as 3D Motion Control Interface for Robotic Manipulator

Tao Chen,[†,‡,§,#] Qiongfeng Shi,[‡,§,⊥,#] Minglu Zhu,[‡,§,⊥,∥] Tianyiyi He,[‡,§,⊥,∥] Lining Sun,[†] Lei Yang,[*,¶] and Chengkuo Lee[*,‡,§,⊥,∥]

[†]Jiangsu Provincial Key Laboratory of Advanced Robotics, School of Mechanical and Electric Engineering & Collaborative Innovation Center of Suzhou Nano Science and Technology, Soochow University, Suzhou, People's Republic of China 215123
[‡]Department of Electrical and Computer Engineering, National University of Singapore, 4 Engineering Drive 3, Singapore 117576
[§]Center for Intelligent Sensors and MEMS, National University of Singapore, E6 #05-11F, 5 Engineering Drive 1, Singapore 117608
[⊥]Hybrid-Integrated Flexible (Stretchable) Electronic Systems Program, National University of Singapore, E6 #05-4, 5 Engineering Drive 1, Singapore 117608
[∥]NUS Suzhou Research Institute (NUSRI), Suzhou Industrial Park, Suzhou, People's Republic of China 215123
[¶]Orthopaedic Insititute and Department of Orthopaedics, Soochow University, Suzhou, People's Republic of China 215006

Supporting Information

ABSTRACT: **Triboelectric nanogenerators and sensors can be applied as human−machine interfaces to the next generation of intelligent and interactive products, where flexible tactile sensors exhibit great advantages for diversified applications such as robotic control. In this paper, we present a self-powered, flexible, triboelectric sensor (SFTS) patch for finger trajectory sensing and further apply the collected information for robotic control. This innovative sensor consists of flexible and environmentally friendly materials, *i.e.*, starch-based hydrogel, polydimethylsiloxane (PDMS), and silicone rubber. The sensor patch can be divided into a two-dimensional (2D) SFTS for in-plane robotic movement control and a one-dimensional (1D) SFTS for out-of-plane robotic movement control. The 2D-SFTS is designed with a grid structure on top of the sensing surface to track the continuous sliding information on the fingertip, *e.g.*, trajectory, velocity, and acceleration, with four circumjacent starch-based hydrogel PDMS elastomer electrodes. Combining the 2D-SFTS with the 1D-SFTS, three-dimensional (3D) spatial information can be generated and applied to control the 3D motion of a robotic manipulator, and the real-time demonstration is successfully realized. With the facile design and very low-cost materials, the proposed SFTS shows great potential for applications in robotics control, touch screens, and electronic skins.**

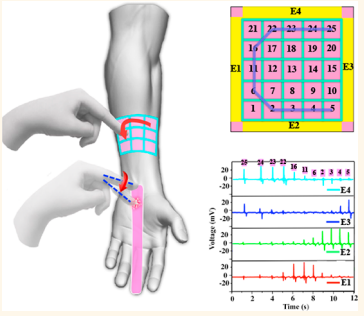

KEYWORDS: *triboelectric effect, self-powered, wearable, flexible, robot*

Wearable sensors have been an attractive research topic and have received tremendous research effort in the past few years.[1−4] For example, W. Gao *et al.* carried out a prominent study on wearable and effective sweat sensors in the development of personalized healthcare devices.[1] B. C. K. Tee *et al.* reported a wearable skin-inspired mechanoreceptor that can transduce pressure information into frequency signals, marking one step forward to the realization of electronic skin with neural-integrated feedback.[3] Among various wearable applications, tactile sensing and pressure sensing in wearable sensors are important research areas.[5,6] To date, most of the reported tactile sensors are aiming at healthcare and gaming control.[7−12] With respect to the Internet of Things (IoT) and factory automation, the applications of tactile sensors remain to be further studied and expanded. With the development of modern technology and the increasing needs of the IoT, the next-generation robots are designed to work autonomously in a smart factory and operate in a harsh environment, where they can feel and interpret the environment with the help of all kinds of sensors.[13−18] In terms of the applications of tactile sensors, they are mainly used for pressure sensing and collision detection in the process of robot manipulation based on a capacitive mechanism or a piezoresistive mechanism.[19−21] More importantly, a common limitation is that most of these sensors require an external power source. In recent years, a

Received: September 3, 2018
Accepted: October 16, 2018
Published: October 16, 2018

DOI: 10.1021/acsnano.8b06747
ACS Nano 2018, 12, 11561−11571

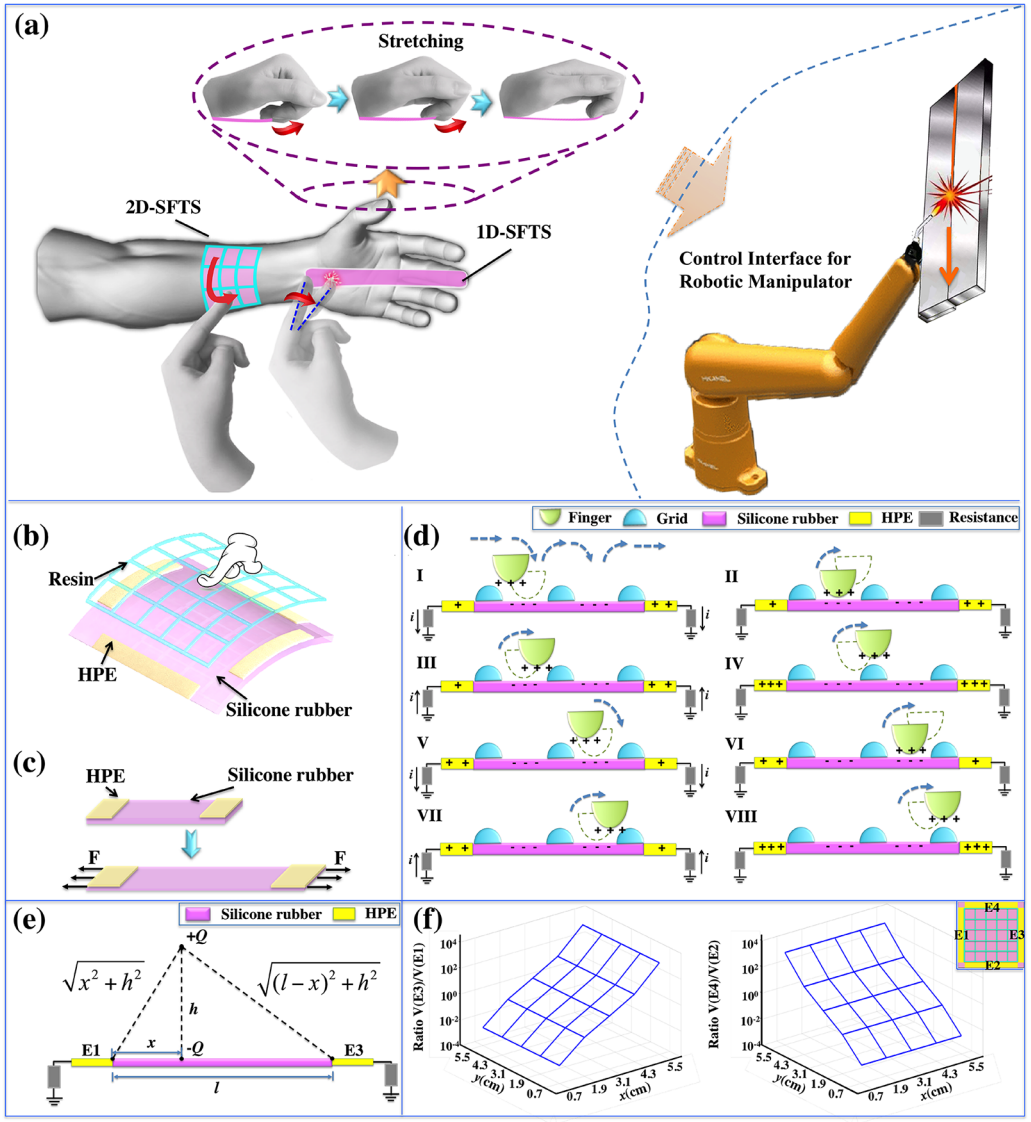

Figure 1. Conceptual illustration and working principle of the wearable flexible patches. (a) 2D-SFTS attached on the arm as a 2D sensing and testing patch. The two ends of the 1D-SFTS are fixed on the wrist and fingers, respectively, and 1D displacement and movement detection is carried out by the stretching action of the fingers. The combination of the two patches can realize 3D motion control of the robot, such as handling, welding, and other operations. (b) Schematic diagram of the 2D-SFTS patch. (c) Schematic diagram of the 1D-SFTS patch. (d) Illustration of the working principle of the gridded 2D-SFTS patch. (e) Electrostatic analysis of the contact process. (f) Voltage ratio of electrode 3 (E3) and electrode 1 (E1) with the location of charges changing, and voltage ratio of electrode 4 (E4) and electrode 2 (E2) with the location of charges changing.

number of self-powered sensors based on triboelectric nanogenerators (TENGs) were introduced.[22−29] TENGs can function as active sensors for detecting pressure changes without the use of an external power source, which has potential applications as self-powered tactile sensors.[30−37] In addition, complex electric circuits can be avoided in these self-powered devices.[38−43] Wang's group integrated the developed tribo-skins with soft actuators, performing various active sensing and interactive tasks during operation of soft robot finger actuators.[44] X. Zhao *et al.* reported a self-powered and self-adaptive motion sensor to detect and recognize various motion behaviors of a robot.[45] In the electronics industry and intelligent robot applications, triboelectric-based self-powered sensors distinguish themselves from others because of their simple structure, flexible nature, cost-effectiveness, and self-powered functionality.[46−49]

On the other hand, tactile sensor arrays have also been widely developed and investigated for different applications. F. Yi *et al.* reported a self-powered 4 × 4 triboelectric sensor array structured with grounded electrodes to monitor two-dimensional (2D) movement of a rolling ball on this array.[50] X. Wang *et al.* fabricated a flexible and stretchable 8 × 8 triboelectric sensor array using polydimethylsiloxane (PDMS) and a Ag nanofiber electrode. Controlling a moving object in the Pac-Man game is demonstrated by drawing a trajectory pattern on this 8 × 8 triboelectric sensor array.[51] Briefly speaking, using a tactile sensor array to detect a trajectory pattern made by fingertips or moving objects on the surface of a tactile sensor array offers a way of controlling objects in cyberspace. Furthermore, H. Wang *et al.* presented a triboelectric keyboard for individual stimulation of sciatic nerves through implanted electrodes.[52] This work indicates

DOI: 10.1021/acsnano.8b06747
ACS Nano 2018, 12, 11561−11571

another interesting application where a tactile sensor array becomes the interface between humans and prosthetics. Regarding the human−robot interaction, the instruction information provided by the control terminal is expected to be used to control the manipulator of a robot in real time. With the triboelectric tactile sensor array demonstrated by X. Wang *et al.*,[51] it is very likely that people can extract and detect the trajectory information from the 64 electrodes' output associated with the 8 × 8 pixels when the user traces a pattern, then further apply such information for robotic manipulation. However, for tactile sensors, a higher resolution and more targets for location usually require an increased number of sensing units and electrode terminals, which will noteworthily cause a cost increase and extra difficulties in electrode extraction, signal interference, and data processing. To address this issue, an analogous method provides a strategy, especially in terms of reducing the number of sensing units and electrodes.[53] As a promising solution, a simplified tactile sensor configuration has been developed, where the position of a fingertip engaged on the tactile sensor surface can be determined by the output ratio from two pairs of electrodes. This pioneer work has been reported by Zhang's group and Wang's group as a self-powered analogue smart skin.[54−56] Leveraging this mechanism, a sizable output power of 10 mW is reported by a multilayered triboelectric touch pad.[57] However, the working mechanism of these tactile sensors depends on the contact−separation of a single touch point, which means that the fingertip has to be separated from the tactile sensor surface after each individual engagement to detect the touch position. Clearly speaking, detection of a continuous 2D trajectory of a moving object or 2D pattern drawn by a fingertip is not possible by this method.

Furthermore, the motion control and accurate position control of a robotic manipulator must have three-dimensional (3D) spatial information, *e.g.*, coordination in three axes. So far, there is no reported work of a tactile sensor array or self-powered analogue smart skin to generate 3D spatial information. In this paper, we present a 2D self-powered, flexible, triboelectric sensor (2D-SFTS) patch for detection of a 2D trajectory drawn by a fingertip. Together with a 1D-SFTS patch, we bring in the position information along the *z*-axis, *i.e.*, vertical axis, to superimpose on sensory information collected from the 2D-SFTS patch as an integrated 3D information platform as a human−machine control interface to control the 3D manipulation of a robot. This important breakthrough is made possible by integrating a grid structure on a silicone rubber surface with two pairs of stretchable electrodes made of a mixture of PDMS and a starch-based hydrogel to form the SFTS. The information on the physical parameters of trajectory, velocity, and acceleration associated with the fingertip addressed on silicone rubber can be measured. Then robotic manipulation is demonstrated in this work as a function of these physical parameters in a real-time manner. This very cost-effective and facile-designed triboelectric tactile sensor has great potential in wide-ranging applications such as robotics, virtual reality (VR), augmented reality (AR), and healthcare.

RESULTS AND DISCUSSION

The concept of the patch device to provide 3D control information through the integration of the 1D-SFTS and 2D-SFTS patches is shown in Figure 1a. The fabricated TENG-based 2D-SFTS patch consists of a flexible substrate, a grid layer, and four electrodes. The 1D-SFTS patch consists of a flexible substrate and two electrodes. Their structure diagram is demonstrated in Figure 1b and c, respectively. The flexible substrate is made of silicone rubber with good stretchable property. It is also the friction layer to contact with objects in a sliding or touching manner. The grid layer made up of resin is deposited on the substrate by 3D printing. Electrodes on the edges of the substrate are fabricated with a starch-based hydrogel PDMS elastomer (HPE), *i.e.*, a mixture of starch-based hydrogel and PDMS. The starch-based hydrogel is obtained by dissolving cornstarch in the electrolyte at 60 °C, and the resultant starch-based hydrogel is maintained at a relative humidity (RH) of 60%, as shown in Supporting Figure S1.

As shown in Figure 1d, the operating mode begins with one contact between the finger and the top of the grid structure. When the finger slides to the right, it approaches the silicone rubber layer from the top of the grid structure shown in Figure 1d-I. Because of the work function difference between skin and silicone rubber, a physical contact between the two dielectric surfaces with distinct electron affinity creates oppositely charged surfaces. There are positive and negative charges on the surface of the finger and silicone rubber layer, respectively. During the approaching process, the positive charges on the finger gradually balance the negative charges on the silicone rubber surface. Therefore, a different amount of charge is forced to flow from each electrode terminal to the ground, thus generating currents while the finger approaches the first contact point on the silicone rubber layer. When the finger contacts the surface of the silicone rubber layer (Figure 1d-II), the electrical field is confined to the space between the finger's surface and the silicone rubber layer so that the electrode voltage will not be affected by the charges on the touch point. When the finger separates and leaves far away from the first contact point on the silicone rubber layer (Figure 1d-III), the negative charges on the surface of the silicone rubber will induce opposite charges on the electrode terminals again. Therefore, currents with different magnitudes from the ground to each electrode terminal will be formed while the finger moves away. When the finger reaches the top of the grid structure, we can conclude that the maximum charge on the electrodes is reached eventually (Figure 1d-IV). When the finger crosses over the grid and approaches the second contact point on the silicone rubber layer (Figure 1d-V), the charges on the two electrode terminals will be repelled and forced to flow into the ground. Therefore, a negative current will be formed, and the above process and phenomenon are repeated. Based on the different current and voltage output of four electrodes, the location of contact can be defined. Benefited from the division of the grid, the continuous sliding trajectory and movement of the finger on the sensor surface are recorded by continuous pixel positions; thus the trajectory, speed, and acceleration of the motion can be further derived.

Since the substrate material and electrode material used by the 1D-SFTS and 2D-SFTS are the same, to obtain the detection characteristics of the patches by an analogous method, the relationship of an output voltage from the opposite electrodes is first studied. The theoretical analysis of electrostatic induction during the contact process is illustrated in Figure 1e. During the process of the finger sliding or touching along the device surface, the electrical fields on the opposite electrodes change accordingly.

DOI: 10.1021/acsnano.8b06747
ACS Nano 2018, 12, 11561−11571

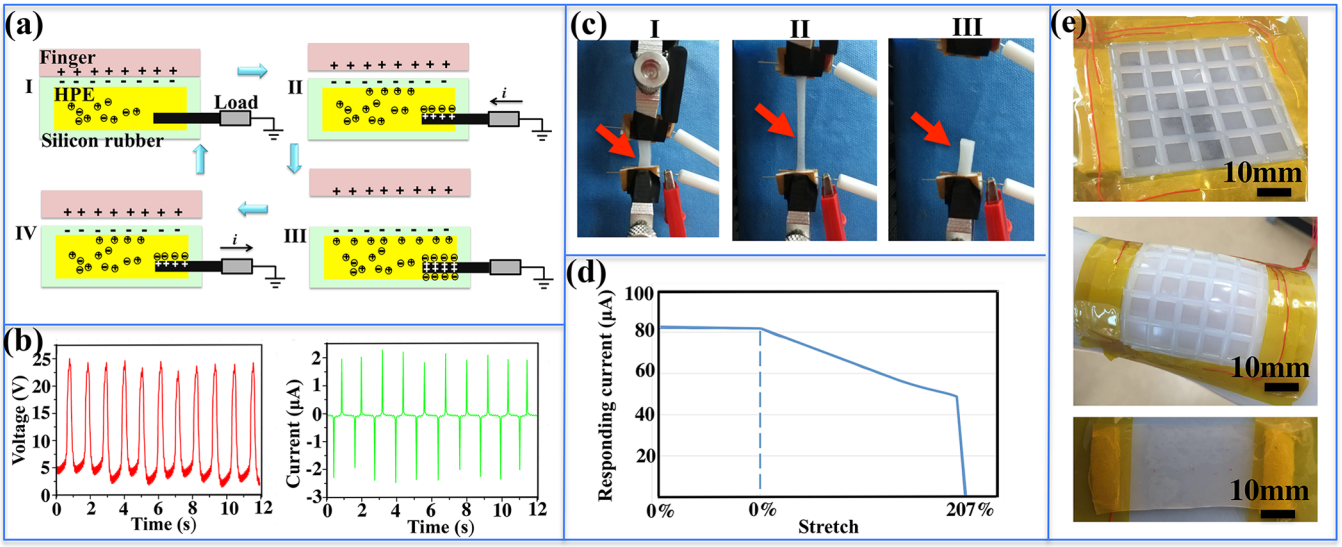

Figure 2. TENG-based working mechanisms of the HPE electrode and the electrical characteristics of the electrode. (a) Schematic illustration of TENG-based working principles of the HPE electrode in single-electrode mode. I: contact state; II: separating state; III: separated state; IV: approaching stage. (b) Open-circuit voltage and short-circuit current of an SFTS based on the HPE electrode. (c) Photographs of a stretching test of HPE and (d) electrical characteristics curve under a voltage of 1.5 V. (e) Photographs of 2D-SFTS and 1D-SFTS patches.

If the electric potential of the ground and infinity is assumed to be 0 V, then the electric potential of a point charge can be written as

$$U = k\frac{Q}{r} \tag{1}$$

where Q is the amount of charge, r is the distance to the point charge, and k is Coulomb's constant.

The distance between two opposite electrodes (E1 and E3) is assumed to be l. After contact with the silicone rubber surface, the finger with a charge of $+Q$ moves away from the silicone rubber surface to a distance of h. The touch point on the silicone rubber surface has a charge of $-Q$, correspondingly. If the distance between the touch point and E1 is x, then the distance between the touch point and E3 is $l - x$. Thus, the electric potentials of E1 and E3 (V_{E1} and V_{E3}) can be expressed as

$$\begin{cases} V_{E1} = k\dfrac{Q}{\sqrt{x^2 + h^2}} - k\dfrac{Q}{x} \\ V_{E3} = k\dfrac{Q}{\sqrt{(l-x)^2 + h^2}} - k\dfrac{Q}{l-x} \end{cases} \tag{2}$$

Their ratio can be then derived as

$$\frac{V_{E3}}{V_{E1}} = \frac{k\frac{Q}{\sqrt{(l-x)^2+h^2}} - k\frac{Q}{l-x}}{k\frac{Q}{\sqrt{x^2+h^2}} - k\frac{Q}{x}} = \frac{\frac{1}{\sqrt{(l-x)^2+h^2}} - \frac{1}{l-x}}{\frac{1}{\sqrt{x^2+h^2}} - \frac{1}{x}} \tag{3}$$

The ratio is only dependent on the touch point position, *i.e.*, x, if l and h remain constant. More importantly, the ratio is irrelevant of the amount of charge, which enables stable and reliable position sensing of the device even under different contact force and RH. The same relationship between V_{E2} and V_{E4} can be obtained using the same procedures. Due to the grid structure, the distance h is constant. Supposing that h is 1.5 mm, Figure 1f shows the simulation result of V_{E3}/V_{E1} and V_{E4}/V_{E2} of the four-electrode device, respectively, while the charge location changes. The result shows good monotonicity, which is especially significant for confirming the location of touching.

In order to simplify the structure and improve the flexible and stretchable characteristics, the electrodes of SFTS are made up of HPE. The mechanism is schematically illustrated in Figure 2a. HPE is wrapped around the silicone rubber during the fabrication. When the finger contacts the silicone rubber, contact electrification occurs at the interface due to their different electron affinities. HPE is conductive, and the current through HPE could reflect the changes in the external electric field. Figure 2b shows the open-circuit voltage and short-circuit current of the HPE−silicone rubber device by finger tapping. The HPE is then examined under stretched motion by the linear motor as shown in Figure 2c. In the whole stretching process, the resistance range is about 18−30 KΩ based on the applied voltage of 1.5 V. The electrical characteristics curve is shown in Figure 2d. It can be seen that the electrode material still exhibits good electrical conductivity under a stretchable state up to 200% strain. A demonstration and test curves of its electrical conductivity are shown in Supporting Figure S2. Photographs of the fabricated SFTS patches are presented in Figure 2e. The dimensions of the 2D-SFTS are listed in Supporting Table S1. The 1D-SFTS patch will be investigated in terms of different sizes in subsequent experiments.

In view of the structural character of the gridded 2D-SFTS patch, the trajectory detection characteristic is introduced here. Before carrying out the experiment on trajectory detection, the contact points of the continuous pixel are tested and analyzed. To obtain a 2D location for the contact, two voltage ratios from the opposite electrodes (denoted as V_{E3}/V_{E1} and V_{E4}/V_{E2}) are measured with a 5 × 5 test lattice shown in Figure 3a. Measurement for each virtual pixel is repeated 100 times to calculate the average value as the standard contact point in the square area. For each point, 100 groups of the peak output voltages are obtained in advance. As a representative of a common situation, the point distribution graph of the 100 test

DOI: 10.1021/acsnano.8b06747
ACS Nano 2018, 12, 11561−11571

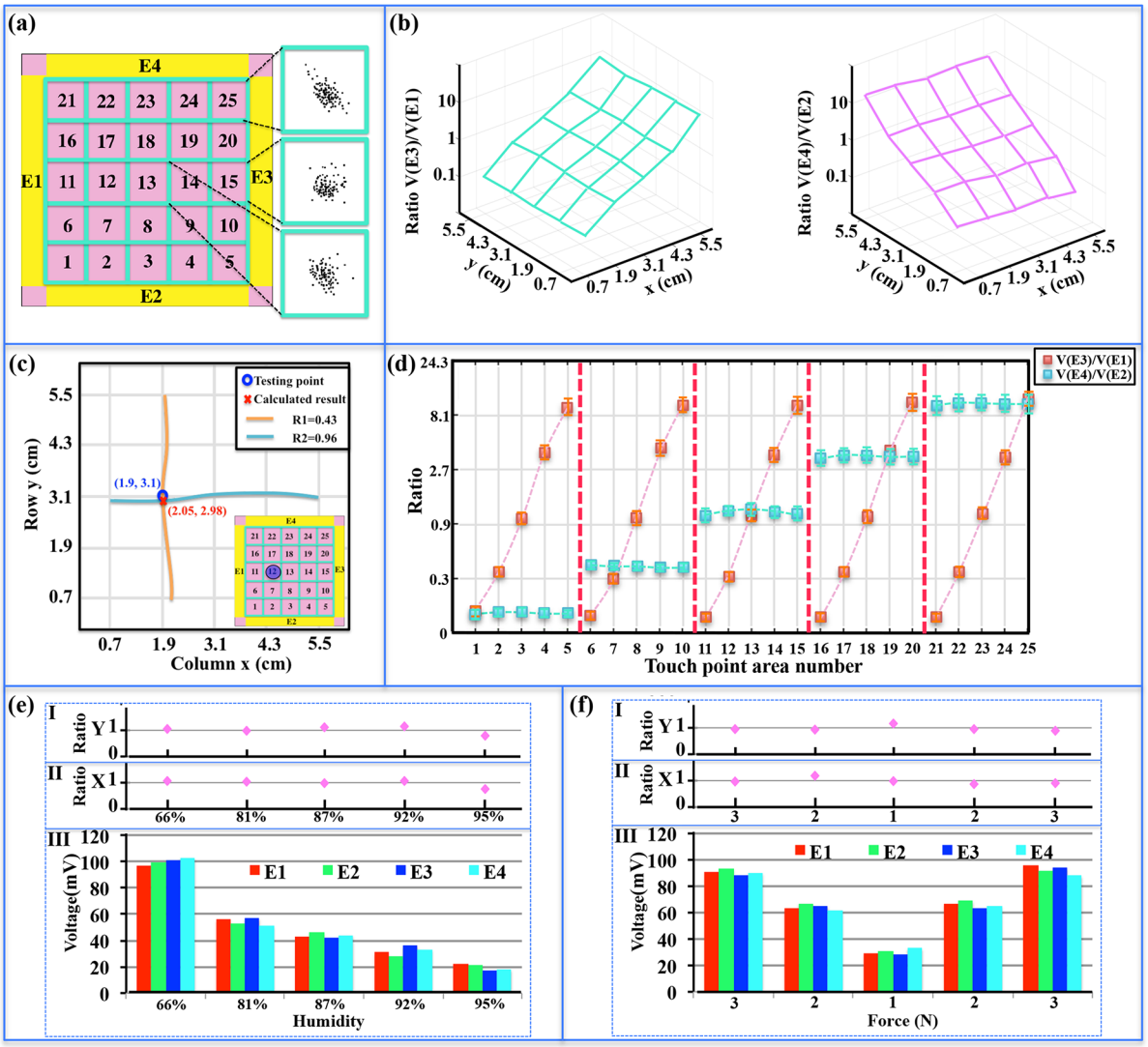

Figure 3. (a) 100 tests of voltage ratios of opposite electrodes at lattices No. 13, No. 15, and No. 25, showing good centrality. (b) Voltage ratios of E3 and E1 with 25 testing points and the voltage ratios of E4 and E2 with 25 testing points. (c) Comparison between the test location and the actual location. (d) Average values and the standard deviation values of the ratios V_{E3}/V_{E1} and V_{E4}/V_{E2} in sequential order. (e) Tests of the 2D-SFTS patch under different humidities. (f) Tests of the 2D-SFTS patch under different forces.

results is shown in Figure 3a at lattices No. 13, No. 15, and No. 25. Because of the restriction of the grid, the finger contact points with silicone rubber are mainly concentrated in the center area of each single lattice. With 100 tests, the outputs are stable and the voltage ratios also show notable aggregation. Then the ratios of $R_1 = V_{E3}/V_{E1}$ and $R_2 = V_{E4}/V_{E2}$ of each group are calculated, as shown in Figure 3b. The average values of the calculated R_1 and R_2 for each touch point are listed in Supporting Tables S2 and S3, respectively. R_1 and R_2 monotonically increase and the voltage ratio trend shows good resolution. To verify the performance of the locating capability of the device, a location test at the center point of single lattice No. 12 is carried out, as shown in Figure 3c. The ratios obtained from the measured output voltages are R_1 = 0.43 and R_2 = 0.96. Two curves corresponding to R_1 and R_2 are plotted, and the intersection point can be calculated as (2.05, 2.98). The distance deviation between the actual touch point and the calculated point is 1.5 mm. Similarly, through experimental testing and calculation by MATLAB, the distance deviations of all 25 points are between 0.02 and 1.60 mm. Therefore, the position-sensing resolution of the points in a single lattice is ~1.6 mm. All the average values and the standard deviation values of the ratios are plotted in Figure 3d. In order to achieve the accuracy and standardization of trajectory monitoring and motion detection, normalization of the average values for each region of the above test is carried out. The ratios obtained can be divided into 25 values for both R_1 and R_2 when the touch point changes. These values are defined as the ratios of the geometric center points of every single lattice. In trajectory measurements, these discrepancies can be eliminated by normalizations. Taking the ring location as an example, the normalization of theoretical ratios and experimental values are illustrated in Supporting Figure S3. In order to check the reliability of the SFTS device, the tests are conducted under different environments and forces as shown in Figure 6e and f. It can be seen that the voltage ratio of the opposite electrodes is stable although the voltage amplitude varies with the change of humidity and force, implying that the ratio method can eliminate external interference. The spray device is used to change the humidity on the surface of the

DOI: 10.1021/acsnano.8b06747
ACS Nano 2018, 12, 11561−11571

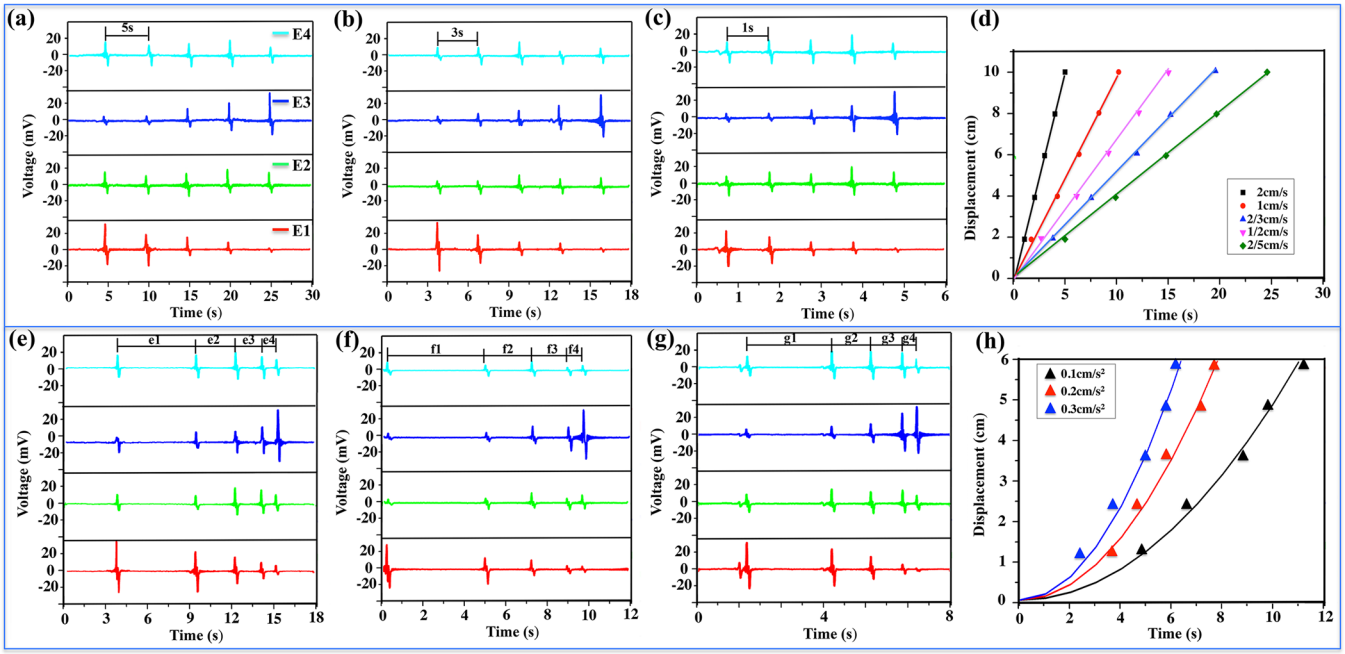

Figure 4. Detection of the velocity and acceleration of an object sliding on the device. (a–c) Measured voltage as an object slides across a path (No. 11 → No. 12 → No. 13 → No. 14 → No. 15) at a preset speed of 2, 2/3, and 2/5 cm/s. (d) Detected displacement of the object over time. (e–g) Measured voltages when an object slides across a path (No. 11 → No. 12 → No. 13 → No. 14 → No. 15) with different accelerations (0.6, 1.2, 3.5 mm/s^2). The intervals of the peak time in (e) are e1 = 6.3 s, e2 = 2.7 s, e3 = 2.0 s, and e4 = 1.7 s, respectively. The intervals of the peak time in (f) are f1 = 4.6 s, f2 = 1.8 s, f3 = 1.4 s, and f4 = 0.7 s, respectively. The intervals of the peak time in (g) are g1 = 2.6 s, g2 = 1.1 s, g3 = 0.8 s, and g4 = 0.6 s, respectively. (h) Detected accelerations of the object by the 2D-SFTS patch.

device. Five groups of experiments are carried out under different humidities. The measured values of surface humidity of the five groups are 66%, 81%, 87%, 92%, and 95%, respectively. In each group, the voltages of four electrodes are detected by tapping the center point (3.1, 3.1) of the 1D-SFTS patch. The average values of electrode voltages of each group (50 times) are calculated and depicted by a column diagram, as shown in Figure 6e-III. The ratios of the tapping point in the x direction and y direction are calculated according to the average values and marked in Figure 6e-I and e-II. It can be seen that with the increase of humidity, the output voltage of the electrode will decrease significantly, but it does not affect the calculated value of the position point. As shown in Figure 6f, five groups of experiments are carried out under different forces. Similarly, the magnitude of the force has a negligible effect on the location calculation.

In the above analysis, the pixel matrix of 5 × 5 is calibrated and the average value of each region voltage is processed. In order to quantitatively characterize the SFTS's response to a motion, *e.g.*, finger sliding through the surface of the sensor, the pixel area touched by the finger records the voltage signal to detect its movement and trajectory. The output voltage signals of the 25 lattice regions are recorded in real time. By addressing and monitoring the positive output voltage signals in the 25 lattice regions, the touch information on the finger can be attained. When the finger slides on the SFTS along one path, the voltage of the region that the finger passes through rises to a peak. In this regard, a 2D contour plot of the values of the output voltage from all electrodes is obtained when the finger gets to the region that explicitly indicates the moving path of the finger, as shown in Supporting Movie S1. Since the interval between two neighboring regions is a constant that was determined when constructing the grid structure, the location of the object can be recognized easily. More importantly, the trajectory, velocity, and acceleration of the object can be derived through analysis and calculation. The 2D-SFTS patch is fixed on the platform of a linear motor, and the characteristic is calibrated by setting a different speed of the linear motor. In the experiment, the patch is moving with the motor and the finger are stationary relative to the ground. Figure 4a–c show the measured results of the voltage when the finger slides on the 2D-SFTS patch with different velocities. By simply dividing the distance between two regions by the time taken to cover the distance, the velocity from one electrode to another can be derived. The displacement of the finger sliding with time can be easily derived, which is presented in Figure 4d. Figure 4e–g exhibit the ability of the 2D-SFTS to detect accelerated motion of the finger sliding with different accelerations. The ratios of the opposite voltages in the figure can calculate the trajectory of the finger sliding, and the acceleration of the motion can be calculated combined with the voltage interval time. The displacement of the finger sliding with time can be easily derived, which is presented in Figure 4h. Because the velocity and acceleration of the 2D-SFTS patch are preset by the linear motor, the calculated velocity and acceleration are basically in agreement with the preset value, ignoring the influence of the slight jitter of the finger.

The above sections mainly discuss the characteristic testing of the 2D-SFTS patch. Based on a similar analogous locating method, we propose a stretchable 1D-SFTS patch. The E1 end of the 1D-SFTS patch is fixed, while the E2 end is movable subjected to tensile stress (Figure 5a). When knocking a point with constant distance to E1 on the patch, a voltage ratio of the two electrodes (V_{E2}/V_{E1}) can be obtained through Figure 1e and eq 3. When the patch is stretched to a certain distance, the voltage ratio decreases when we knock on the same point with

DOI: 10.1021/acsnano.8b06747
ACS Nano 2018, 12, 11561–11571

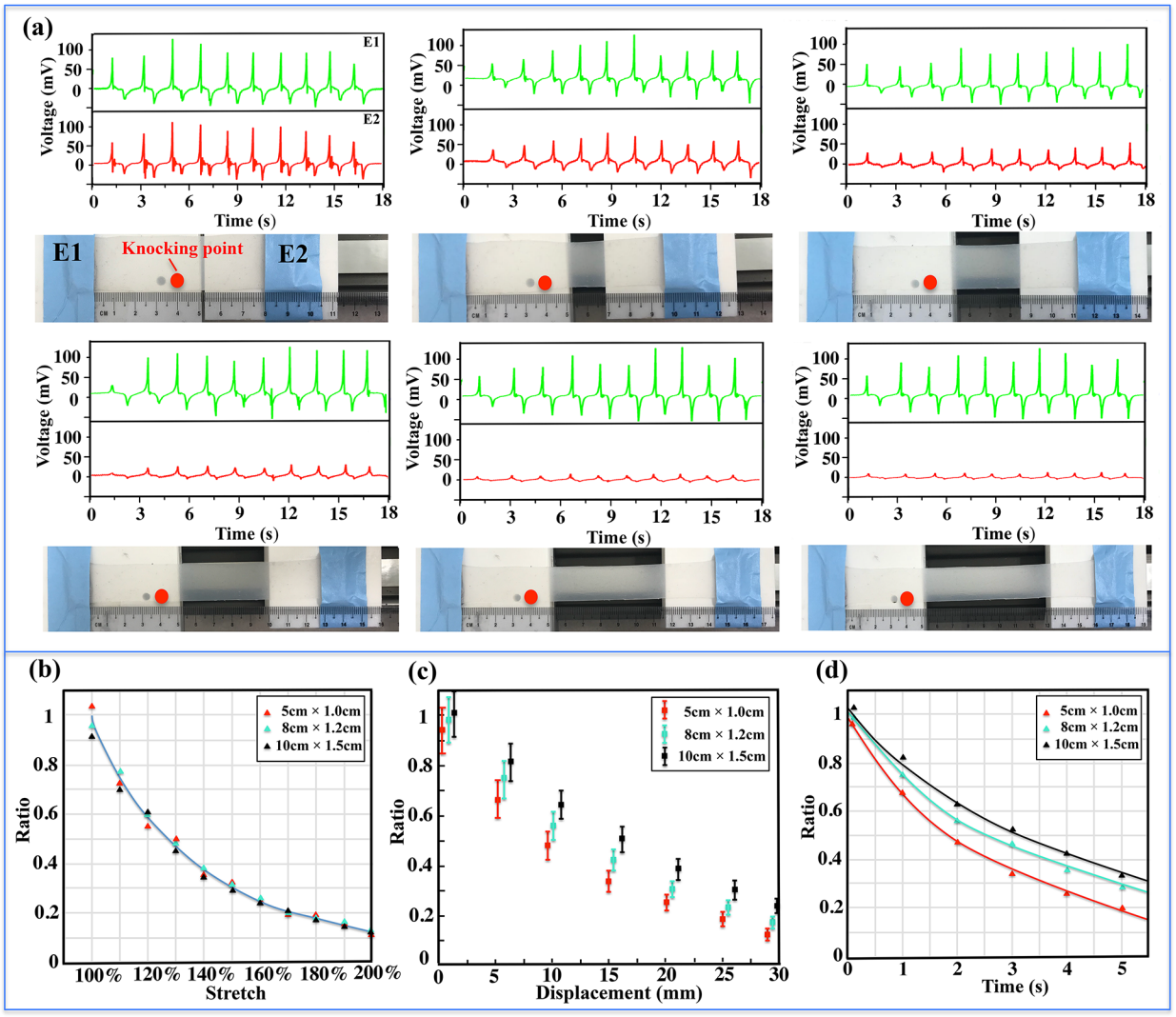

Figure 5. Electrical measurements of a finger knocking on the silicone rubber layer and analysis of the stretch process. (a) Voltage waveform of the two electrode voltages with the increase of the stretch length. (b) Ratio change trend of the two electrodes' voltages with the change of the stretch percentage. (c) Relationship of the error bars of V_{E2}/V_{E1} with the stretch displacement corresponding to different initial lengths. (d) Relationship of the two electrodes' voltage ratio and time at the same stretch speed.

a constant distance relative to the E1 position. The ratio further decreases with increasing stretch length. Based on this phenomenon, the stretch length of the E2 end can be measured by knocking a fixed point relative to E1. That is to say, it can measure the stretch displacement and stretch velocity/acceleration of the E2 end with fixed knocking frequency. The photographs of the 1D-SFTS under different operating conditions demonstrate the stretchable capability of the device as shown in Figure 5a. In the experiment, three different sizes of the patch are investigated in terms of the output voltage ratio. The ratio change trend of two electrode voltages is shown in Figure 5b with the change of the stretch percentage. It can be seen that with the same percentage of stretching, the voltage ratio is basically the same, indicating that the width and thickness of the patch does not affect the output value during stretching. In terms of displacement and velocity detection, we first detected the resolution of stretch displacement. The relationships of the error bars of V_{E2}/V_{E1} with the stretch displacement corresponding to different initial lengths are shown in Figure 5c. The resolution gradually decreases with the increase of stretch length. In addition, the longer the initial length, the faster the resolution decreases. It can be seen that when the stretch displacement is less than 25 mm, the resolution of the three patches is ~5 mm. When the stretch length exceeds 25 mm, the resolution is greater than 5 mm. Therefore, the patch with a shorter initial length is calibrated in terms of the stretch curve in advance for later application. Figure 5d shows the curves of the voltage ratios with time under a stretch speed of 5 mm/s. The 1D-SFTS patch can be stretched to as long as 500%, and the stretchability depends on the type, thickness, and curing extent of the silicone rubber. The curves of the two electrode voltages during the stretching process are shown in Supporting Movie S2.

Furthermore, to check the reliability and long-term stability of the SFTS device, a reliability test is conducted on the 1D-SFTS patch, as shown in Supporting Figure S4, and a long-term stability test is conducted as shown in Supporting Figure S5. Similar to the 2D-SFTS patch, the influence of humidity and force on the 1D-SFTS patch can be ignored. As shown in Supporting Figure S5, there is no significant change of ratios of

DOI: 10.1021/acsnano.8b06747
ACS Nano 2018, 12, 11561−11571

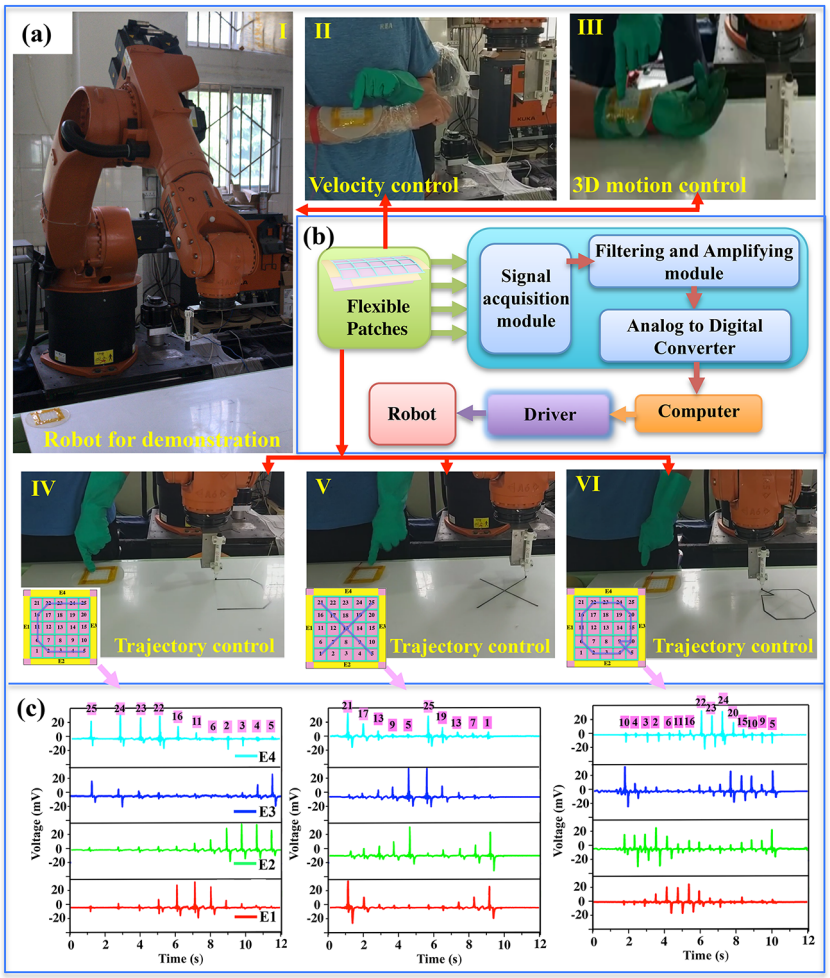

Figure 6. Robotic control schematic diagram and experimental results. (a) Photograph of the robot used in the demonstration. Photographs demonstrating the velocity control, trajectory control, and 3D motion control. (b) Flowchart and system structure of the robotic control demonstration. (c) Voltage curves of four electrodes when a finger slides on the SFTS with "C", "X", and "Q" trajectories. The robotic manipulator demonstrates letter writing on the whiteboard through the flexible patch control. The top of each figure shows the number corresponding to each lattice when the finger slides across.

opposite electrodes after testing for 5000 cycles, which indicates a stable and durable electrical property of the SFTS.

As discussed above, the 1D-SFTS and 2D-SFTS patches can realize trajectory, displacement, and velocity detection. Therefore, the combination of the two patches can achieve 3D signal detection and control. This concept can be applied to the applications of robotics, electronic skins, automatic control, *etc.* To evaluate the characteristics of the SFTS patches and verify the 3D control concept, a robotics control system is developed. Figure 6a shows the robot and the different motion behavior control, such as velocity control, trajectory control, and 3D motion control. The control system includes the SFTS device, a signal acquisition system, a computer, a drive system, and a robot (Figure 6b). Through the control connection between the SFTS patches and the robotic manipulator, experiments at different sliding speeds are conducted first to control the robotic manipulator with different moving speed, as shown in Supporting Movie S3. Then the trajectory tracking ability of the SFTS patch is utilized to control the robotic manipulator to write different letters. Three letters, "C", "X", and "Q" are selected and written by the robot manipulator on a whiteboard, as shown in Supporting Movie S4. Figure 6c illustrates the voltage curves of four electrodes corresponding to the letter trajectories induced by a fingertip. Next the combination of the two patches is demonstrated to realize the 3D motion control of the robot manipulator, as shown in Supporting Movie S5. Therefore, according to the demonstrations, the SFTS patches can work as 3D motion control interfaces for a robotic manipulator in diversified multifunction operations, such as handling operations, welding, and spraying.

CONCLUSIONS

In summary, a self-powered flexible triboelectric sensor patch for trajectory and fingertip motion sensing is proposed and investigated with complete theoretical model and experimental characterization. This very cost-effective and facile-designed sensor is fabricated with environmentally friendly materials, *i.e.*, a starch-based hydrogel, PDMS, and silicone rubber. With the design of a grid structure on top of the triboelectric functional layer, detection of trajectory, velocity, and acceleration of a fingertip moving on the 2D-SFTS can be realized with only four sensing electrodes. Based on an analogous locating method, the 1D-SFTS can measure the 1D stretch displacement and stretch velocity. The combination of the two patches can achieve 3D motion control of a robotic manipulator. These results indicate that the SFTS patches can be adopted as a

DOI: 10.1021/acsnano.8b06747
ACS Nano 2018, 12, 11561−11571

wearable control interface for a robotic manipulator ranging from 1D to 3D applications. With the facile design and very low-cost materials, the developed stretchable flexible triboelectric sensor shows great potential for applications in robotics control, VR, AR, healthcare, *etc.*

METHODS

Fabrication of Carbohydrate-Based Elastomer. Liquid PDMS was prepared by mixing a silicone elastomer base and cross-linker (Sylgard 184, Dow Corning) at a mass ratio of 10:1. Both the starch-based hydrogel and liquid PDMS were degassed in a vacuum chamber to removing gas bubbles in the gel. Then they were mixed together at a volume ratio of 3:1 to obtain the precursor of the carbohydrate-based elastomer. To remove the bubbles in the precursor, the precursor was centrifuged for 10 min at a speed of 3000 rpm. A schematic figure is shown in Supporting Figure S1.

Fabrication of Silicone Rubber and Electrodes. After dispensing the required amounts of parts A and B of the EcoFlex 00-30 into a mixing container (1A:1B by volume), the blend was mixed thoroughly for 3 min and poured into the mold for thin film casting followed by a 20 min baking at 70 °C for curing. The HPE was placed at the corresponding position to form the electrode before the solution solidified, and the position of the HPE was fixed through an external wire until the solution solidified.

Device Fabrication. For the 1D-SFTS patch, three sizes of patches were fabricated in the experiment: 5 cm × 1 cm, 8 cm × 1.2 cm, and 10 cm × 1.5 cm. Their thickness is 2 mm, and the electrode size is 8 mm × 5 mm. For the 2D-SFTS patch, the dimensions are listed in Supporting Table S1.

Device Measurements. The open-circuit voltage and short-circuit current of the electrodes in the patches were measured by a high-impedance electrometer (Keithley 6514). The stretch test was conducted with a linear motor. The morphology of the silicone rubber was measured by field emission scanning electron microscopy (FESEM FEI Verios460).

ASSOCIATED CONTENT

Supporting Information

The Supporting Information is available free of charge on the ACS Publications website at DOI: 10.1021/acsnano.8b06747.

Figures S1−S5 and notes providing the fabrication of the carbohydrate-based elastomer; electrical conductivity test of HPE; normalization example; stability tests under different humidity and forces conditions; tests of long-term stability; Tables S1−S3 providing the formation of the dimensions of the 2D-SFTS patch; voltage ratios calculations (R_1); voltage ratios calculations (R_2) (PDF)

Movie S1: Demonstration of a finger moving on a 2D-SFTS patch (AVI)

Movie S2: Demonstration of the stretch test of a 1D-SFTS patch (AVI)

Movie S3: Demonstration of velocity control of a robotic manipulator (AVI)

Movie S4: Demonstration of trajectory control (AVI)

Movie S5: Demonstration of 3D motion control of the robotic manipulator (AVI)

AUTHOR INFORMATION

Corresponding Authors

*E-mail: leiy@suda.edu.cn.

*E-mail: elelc@nus.edu.sg.

ORCID

Chengkuo Lee: 0000-0002-8886-3649

Author Contributions

#T. Chen and Q. Shi contributed equally to this work.

Notes

The authors declare no competing financial interest.

ACKNOWLEDGMENTS

This research was funded by The National Key Research and Development Program of China (2018YFB1107602); National Natural Science Foundation of China grants (no. 61673287, no. 81622032); State Key Laboratory of Precision Measuring Technology and Instruments; HIFES Seed Funding-2017-01 grant (R-263-501-012-133) "Hybrid Integration of Flexible Power Source and Pressure Sensors" at the National University of Singapore; Agency for Science, Technology and Research (A*STAR), Singapore, and Narodowe Centrum Badań i Rozwoju (NCBR), and Poland Joint Grant (R-263-000-C91-305) "Chip-Scale MEMS Micro-Spectrometer for Monitoring Harsh Industrial Gases". T.C. is thankful, in particular, for the support from his beautiful wife and lovely newborn daughter. He loves them.

REFERENCES

(1) Gao, W.; Emaminejad, S.; Nyein, H. Y. Y.; Challa, S.; Chen, K.; Peck, A.; Fahad, H. M.; Ota, H.; Shiraki, H.; Kiriya, D.; Lien, D. H.; Brooks, G. A.; Davis, R. W.; Javey, A. Fully Integrated Wearable Sensor Arrays for Multiplexed *in situ* Perspiration Analysis. *Nature* **2016**, *529*, 509−514.

(2) Bariya, M.; Nyein, H. Y. Y.; Javey, A. Wearable Sweat Sensors. *Nat. Electron.* **2018**, *1*, 160−171.

(3) Tee, B. C. K.; Chortos, A.; Berndt, A.; Nguyen, A. K.; Tom, A.; McGuire, A.; Lin, Z. C.; Tien, K.; Bae, W. G.; Wang, H.; Mei, P.; Chou, H. H.; Cui, B.; Deisseroth, K.; Ng, T. N.; Bao, Z. Skin-Inspired Organic Digital Mechanoreceptor. *Science* **2015**, *350*, 313−316.

(4) Cai, G.; Wang, J.; Qian, K.; Chen, J.; Li, S.; Lee, P. S. Extremely Stretchable Strain Sensors Based on Conductive Self-Healing Dynamic Cross-Links Hydrogels for Human-Motion Detection. *Adv. Sci.* **2017**, *4*, 1600190.

(5) Cao, Y.; Li, T.; Gu, Y.; Luo, H.; Wang, S.; Zhang, T. Fingerprint-Inspired Flexible Tactile Sensor for Accurately Discerning Surface Texture. *Small* **2018**, *14*, 1703902.

(6) Kim, H.; Ahn, J. H. Graphene for Flexible and Wearable Device Applications. *Carbon* **2017**, *120*, 244−257.

(7) Tok, J. B. H.; Bao, Z. Recent Advances in Flexible and Stretchable Electronics, Sensors and Power Sources. *Sci. China: Chem.* **2012**, *55*, 718−725.

(8) Kang, M.; Kim, J.; Jang, B.; Chae, Y.; Kim, J. H.; Ahn, J. H. Graphene-Based Three Dimensional Capacitive Touch Sensor for Wearable Electronics. *ACS Nano* **2017**, *11*, 7950.

(9) Lipomi, D. J.; Vosgueritchian, M.; Tee, B. C. K.; Hellstrom, S. L.; Lee, J. A.; Fox, C. H.; Bao, Z. Skin-Like Pressure and Strain Sensors Based on Transparent Elastic Films of Carbon Nanotubes. *Nat. Nanotechnol.* **2011**, *6*, 788−792.

(10) Kim, H.; Kim, G.; Kim, T.; Lee, S.; Kang, D.; Hwang, M.; Chae, Y.; Kang, S.; Lee, H.; Park, H.; Shim, W. Transparent, Flexible, Conformal Capacitive Pressure Sensors with Nanoparticles. *Small* **2018**, *14*, 1703432.

(11) Takei, K.; Takahashi, T.; Ho, J. C.; Ko, H.; Gillies, A. G.; Leu, P. W.; Fearing, R. S.; Javey, A. Nanowire Active-Matrix Circuitry for Low-Voltage Macroscale Artificial Skin. *Nat. Mater.* **2010**, *9*, 821−826.

(12) Sekitani, T.; Yokota, T.; Zschieschang, U.; Klauk, H.; Bauer, S.; Takeuchi, K.; Takamiya, M.; Sakurai, T.; Someya, T. Organic Nonvolatile Memory Transistors for Flexible Sensor Arrays. *Science* **2009**, *326*, 1516−1519.

(13) Zhang, Y.; Zhang, F.; Yan, Z.; Ma, Q.; Li, X.; Huang, Y.; Rogers, J. A. Printing, Folding and Assembly Methods for Forming

DOI: 10.1021/acsnano.8b06747
ACS Nano 2018, 12, 11561−11571

3D Mesostructures in Advanced Materials. *Nat. Rev. Mater.* **2017**, *2*, 17019.
(14) Jie, Y.; Jia, X.; Zou, J.; Chen, Y.; Wang, N.; Wang, Z. L.; Cao, X. Natural Leaf Made Triboelectric Nanogenerator for Harvesting Environmental Mechanical Energy. *Adv. Energy Mater.* **2018**, *8*, 1703133.
(15) Gong, S.; Schwalb, W.; Wang, Y.; Chen, Y.; Tang, Y.; Si, J.; Shirinzadeh, B.; Cheng, W. A Wearable and Highly Sensitive Pressure Sensor with Ultrathin Gold Nanowires. *Nat. Commun.* **2014**, *5*, 3132.
(16) Wang, H.; Pastorin, G.; Lee, C. Toward Self-Powered Wearable Adhesive Skin Patch with Bendable Microneedle Array for Transdermal Drug Delivery. *Adv. Sci.* **2016**, *3*, 1500441.
(17) Ma, Y.; Feng, X.; Rogers, J. A.; Huang, Y.; Zhang, Y. Design and Application of 'J-Shaped' Stress−Strain Behavior in Stretchable Electronics: a Review. *Lab Chip* **2017**, *17*, 1689−1704.
(18) Wang, J.; Cai, G.; Li, S.; Gao, D.; Xiong, J.; Lee, P. S. Printable Superelastic Conductors with Extreme Stretchability and Robust Cycling Endurance Enabled by Liquid-Metal Particles. *Adv. Mater.* **2018**, *30*, 1706157.
(19) Moisio, S.; León, B.; Korkealaakso, P.; Morales, A. Model of Tactile Sensors Using Soft Contacts and Its Application in Robot Grasping Simulation. *Robot. Auto. Syst.* **2013**, *61*, 1−12.
(20) Wu, Y.; Karakurt, I.; Beker, L.; Kubota, Y.; Xu, R.; Ho, K. Y.; Zhao, S.; Zhong, J.; Zhang, M.; Wang, X.; Lin, L. Piezoresistive Stretchable Strain Sensors with Human Machine Interface Demonstrations. *Sens. Actuators, A* **2018**, *279*, 46−52.
(21) Makihata, M.; Muroyama, M.; Tanaka, S.; Nakayama, T.; Nonomura, Y.; Esashi, M. Design and Fabrication Technology of Low Profile Tactile Sensor with Digital Interface for Whole Body Robot Skin. *Sensors* **2018**, *18*, 2374.
(22) Yang, W.; Chen, J.; Zhu, G.; Yang, J.; Bai, P.; Su, Y.; Jing, Q.; Cao, X.; Wang, Z. L. Harvesting Energy from the Natural Vibration of Human Walking. *ACS Nano* **2013**, *7*, 11317−11324.
(23) Kim, S.; Gupta, M. K.; Lee, K. Y.; Sohn, A.; Kim, T. Y.; Shin, K. S.; Kim, D.; Kim, S. K.; Lee, K. H.; Shin, H. J.; Kim, D. W.; Kim, S. W. Transparent Flexible Graphene Triboelectric Nanogenerators. *Adv. Mater.* **2014**, *26*, 3918−3925.
(24) Chen, B.; Yang, Y.; Wang, Z. L. Scavenging Wind Energy by Triboelectric Nanogenerators. *Adv. Energy Mater.* **2018**, *8*, 1702649.
(25) Zhang, R.; Hummelgård, M.; Örtegren, J.; Olsen, M.; Andersson, H.; Yang, Y.; Olin, H. Human Body Constituted Triboelectric Nanogenerators as Energy Harvesters, Code Transmitters, and Motion Sensors. *ACS Appl. Energy Mater.* **2018**, *1*, 2955−2960.
(26) Chen, J.; Yang, J.; Li, Z.; Fan, X.; Zi, Y.; Jing, Q.; Guo, H.; Wen, Z.; Pradel, K. C.; Niu, S.; Wang, Z. L. Networks of Triboelectric Nanogenerators for Harvesting Water Wave Energy: A Potential Approach toward Blue Energy. *ACS Nano* **2015**, *9*, 3324−3331.
(27) Ma, Y.; Zheng, Q.; Liu, Y.; Shi, B.; Xue, X.; Ji, W.; Liu, Z.; Jin, Y.; Zou, Y.; An, Z.; Zhang, W.; Wang, X.; Jiang, W.; Xu, Z.; Wang, Z. L.; Li, Z.; Zhang, H. Self-Powered, One-Stop, and Multifunctional Implantable Triboelectric Active Sensor for Real-Time Biomedical Monitoring. *Nano Lett.* **2016**, *16*, 6042−6051.
(28) Choi, H. J.; Lee, J. H.; Jun, J.; Kim, T. Y.; Kim, S. W.; Lee, H. High-Performance Triboelectric Nanogenerators with Artificially Well-Tailored Interlocked Interfaces. *Nano Energy* **2016**, *27*, 595−601.
(29) Zhong, J.; Zhong, Q.; Zang, X.; Wu, N.; Li, W.; Chu, Y.; Lin, L. Flexible PET/EVA-Based Piezoelectric Generator for Energy Harvesting in Harsh Environments. *Nano Energy* **2017**, *37*, 268−274.
(30) Chen, S.; Cao, X.; Wang, N.; Ma, L.; Zhu, H.; Willander, M.; Jie, Y.; Wang, Z. L. An Ultrathin Flexible Single-Electrode Triboelectric-Nanogenerator for Mechanical Energy Harvesting and Instantaneous Force Sensing. *Adv. Energy Mater.* **2017**, *7*, 1601255.
(31) Wang, H.; Wu, H.; Hasan, D.; He, T.; Shi, Q.; Lee, C. Self-Powered Dual-Mode Amenity Sensor Based on the Water-Air Triboelectric Nanogenerator. *ACS Nano* **2017**, *11*, 10337−10346.
(32) Hassani, F. A.; Mogan, R. P.; Gammad, G. G. L.; Wang, H.; Yen, S. C.; Thakor, N. V.; Lee, C. Toward a Self-Control System for a Neurogenic Underactive Bladder − A Triboelectric Nanogenerator Sensor Integrated with a Bi-Stable Micro-Actuator. *ACS Nano* **2018**, *12*, 3487−3501.
(33) Chen, B.; Yang, N.; Jiang, Q.; Chen, W.; Yang, Y. Transparent Triboelectric Nanogenerator-induced High Voltage Pulsed Electric Field for a Self-Powered Handheld Printer. *Nano Energy* **2018**, *44*, 468−475.
(34) Liu, G.; Chen, J.; Guo, H.; Lai, M.; Pu, X.; Wang, X.; Hu, C. Triboelectric Nanogenerator Based on Magnetically Induced Retractable Spring Steel Tapes for Efficient Energy Harvesting of Large Amplitude Motion. *Nano Res.* **2018**, *11*, 633−641.
(35) Cao, R.; Pu, X.; Du, X.; Yang, W.; Wang, J.; Guo, H.; Zhao, S.; Yuan, Z.; Zhang, C.; Li, C.; Wang, Z. L. Screen-Printed Washable Electronic Textiles as Self-Powered Touch/Gesture Tribo-Sensors for Intelligent Human−Machine Interaction. *ACS Nano* **2018**, *12*, 5190−5196.
(36) Wang, Y.; Yang, Y.; Wang, Z. L. Triboelectric Nanogenerators as Flexible Power Sources. *npj Flex. Electron.* **2017**, *10*, 1−10.
(37) Hassani, F. A.; Lee, C. A Triboelectric Energy Harvester Using Low-Cost, Flexible, and Biocompatible Ethylene Vinyl Acetate (EVA). *J. Microelectromech. Syst.* **2015**, *24*, 1338−1345.
(38) Yang, Y.; Zhou, Y. S.; Zhang, H.; Liu, Y.; Lee, S.; Wang, Z. L. A Single-Electrode Based Triboelectric Nanogenerator as Self-Powered Tracking System. *Adv. Mater.* **2013**, *25*, 6594−6601.
(39) Liu, H.; Ji, Z.; Xu, H.; Sun, M.; Chen, T.; Sun, L.; Chen, G.; Wang, Z. Large-Scale and Flexible Self-Powered Triboelectric Tactile Sensing Array for Sensitive Robot Skin. *Polymers* **2017**, *9*, 586.
(40) Fan, F. R.; Lin, L.; Zhu, G.; Wu, W. Z.; Zhang, R.; Wang, Z. L. Transparent Triboelectric Nanogenerators and Self-Powered Pressure Sensors Based on Micropatterned Plastic Films. *Nano Lett.* **2012**, *12*, 3109−3114.
(41) Yang, Y.; Zhang, H.; Lin, Z. H.; Zhou, Y. S.; Jing, Q.; Su, Y.; Yang, J.; Chen, J.; Hu, C.; Wang, Z. L. Human Skin Based Triboelectric Nanogenerators for Harvesting Biomechanical Energy and as Self-Powered Active Tactile Sensor System. *ACS Nano* **2013**, *7*, 9213−9222.
(42) Cheng, X.; Miao, L.; Song, Y.; Su, Z.; Chen, H.; Chen, X.; Zhang, J.; Zhang, H. High Efficiency Power Management and Charge Boosting Strategy for a Triboelectric Nanogenerator. *Nano Energy* **2017**, *38*, 438−446.
(43) Chen, H.; Su, Z.; Song, Y.; Cheng, X.; Chen, X.; Meng, B.; Song, Z.; Chen, D.; Zhang, H. Omnidirectional Bending and Pressure Sensor Based on Stretchable CNT-PU Sponge. *Adv. Funct. Mater.* **2017**, *27*, 1604434.
(44) Lai, Y. C.; Deng, J.; Liu, R.; Hsiao, Y. C.; Zhang, S. L.; Peng, W.; Wu, H. M.; Wang, X.; Wang, Z. L. Actively Perceiving and Responsive Soft Robots Enabled by Self-Powered, Highly Extensible, and Highly Sensitive Triboelectric Proximity- and Pressure-Sensing Skins. *Adv. Mater.* **2018**, *30*, 1801114.
(45) Zhao, X.; Kang, Z.; Liao, Q.; Zhang, Z.; Ma, M.; Zhang, Q.; Zhang, Y. Ultralight, Self-Powered and Self-Adaptive Motion Sensor Based on Triboelectric Nanogenerator for Perceptual Layer Application in Internet of Things. *Nano Energy* **2018**, *48*, 312−319.
(46) Zhu, G.; Pan, C. F.; Guo, W. X.; Chen, C.; Zhou, Y. S.; Yu, R. M.; Wang, Z. L. Triboelectric-Generator-Driven Pulse Electrodeposition for Micropatterning. *Nano Lett.* **2012**, *12*, 4960−4965.
(47) Liu, H.; Koh, K. H.; Lee, C. Ultra-Wide Frequency Broadening Mechanism for Micro-Scale Electromagnetic Energy Harvester. *Appl. Phys. Lett.* **2014**, *104*, R175.
(48) Zhong, J. W.; Zhang, Q.; Fan, F. R.; Zhang, Y.; Wang, S. H.; Hu, B.; Wang, Z. L.; Zhou, J. Finger Typing Driven Triboelectric Nanogenerator and Its Use for Instantaneously Lighting up LEDs. *Nano Energy* **2012**, *2*, 491−497.
(49) Wu, Y.; Hu, Y.; Huang, Z.; Lee, C.; Wang, F. Electret-Material Enhanced Triboelectric Energy Harvesting from Air Flow for Self-Powered Wireless Temperature Sensor Network. *Sens. Actuators, A* **2018**, *271*, 364−372.
(50) Yi, F.; Lin, L.; Niu, S.; Yang, J.; Wu, W.; Wang, S.; Liao, Q.; Zhang, Y.; Wang, Z. L. Self-Powered Trajectory, Velocity, and

DOI: 10.1021/acsnano.8b06747
ACS Nano 2018, 12, 11561−11571

Acceleration Tracking of a Moving Object/Body using a Triboelectric Sensor. *Adv. Funct. Mater.* **2015**, *24*, 7488−7494.
(51) Wang, X.; Zhang, Y.; Zhang, X.; Huo, Z.; Li, X.; Que, M.; Peng, Z.; Wang, H.; Pan, C. A Highly Stretchable Transparent Self-Powered Triboelectric Tactile Sensor with Metallized Nanofibers for Wearable Electronics. *Adv. Mater.* **2018**, *30*, 1706738.
(52) Lee, S.; Wang, H.; Wang, J.; Shi, Q.; Cheng, S.; Thakor, N. V.; Lee, C. Battery-Free Neuromodulator for Peripheral Nerve Direct Stimulation. *Nano Energy* **2018**, *50*, 148−158.
(53) Segev-Bar, M.; Konvalina, G.; Haick, H. High-Resolution Unpixelated Smart Patches with Antiparallel Thickness Gradients of Nanoparticles. *Adv. Mater.* **2015**, *27*, 1779−1784.
(54) Shi, M.; Zhang, J.; Chen, H.; Han, M.; Shankaregowda, S. A.; Su, Z.; Meng, B.; Cheng, X.; Zhang, H. Self-Powered Analogue Smart Skin. *ACS Nano* **2016**, *10*, 4083.
(55) Li, T.; Zou, J.; Xing, F.; Zhang, M.; Cao, X.; Wang, N.; Wang, Z. L. From Dual-Mode Triboelectric Nanogenerator to Smart Tactile Sensor: A Multiplexing Design. *ACS Nano* **2017**, *11*, 3950−3956.
(56) Wu, H.; Su, Z.; Shi, M.; Miao, L.; Song, Y.; Chen, H.; Han, M.; Zhang, H. Self-Powered Noncontact Electronic Skin for Motion Sensing. *Adv. Funct. Mater.* **2018**, *28*, 1704641.
(57) Chen, T.; Shi, Q.; Li, K.; Yang, Z.; Liu, H.; Sun, L.; Dziuban, J. A.; Lee, C. Investigation of Position Sensing and Energy Harvesting of a Flexible Triboelectric Touch Pad. *Nanomaterials* **2018**, *8*, 613.

DOI: 10.1021/acsnano.8b06747
ACS Nano 2018, 12, 11561−11571